Short- and medium-range structure synergistically control fracture toughness of densified aluminoborate glasses

Elsebeth J. Pedersen [1], Theany To [1], Søren S. Sørensen [1], Rasmus Christensen [1], Johan F. S. Christensen [1],
Lars R. Jensen [2], Michal Bockowski [3], Oxana V. Magdysyuk [4], Maria Diaz-Lopez [4],
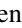Yuanzheng Yue [1], and Morten M. Smedskjaer [1,*]

[1]*Department of Chemistry and Bioscience, Aalborg University, 9220 Aalborg, Denmark*
[2]*Department of Materials and Production, Aalborg University, 9220 Aalborg, Denmark*
[3]*Institute of High-Pressure Physics, Polish Academy of Sciences, 01-142 Warsaw, Poland*
[4]*Diamond Light Source Ltd., Harwell Science and Innovation Campus, Didcot OX11 0DE, United Kingdom*

Methods to improve the fracture toughness of oxide glasses are needed since low fracture toughness is a major bottleneck for their applications. To overcome this, it is critically important to investigate the effect of both short- and medium-range structural features on fracture toughness. Recent work reported a record-high fracture toughness for a bulk lithium aluminoborate glass subjected to hot compression. Here, we further explore the structural origin of this high fracture toughness by subjecting different alkali aluminoborate glasses to hot compression. Through a combination of x-ray total scattering experiments and atomistic simulations, we find that hot compression causes significant changes to both the short- and medium-range order structure of the glasses, e.g., increased coordination numbers (CNs) of network forming species and decreased average size of ring-type structures. To this end, we reveal positive correlations between the pressure-induced increase in fracture toughness and (i) the increase in average CN of network forming species and (ii) the area of the first sharp diffraction peak in the structure factor. Our study thus improves the understanding of which structural features benefit intrinsic toughening of oxide glasses.

I. INTRODUCTION

The brittle nature of oxide glasses remains a main limiting factor for their applications and simultaneously prevents the environmental footprint of their production from being significantly lowered [1]. Fractures of oxide glasses often start from preexisting surface flaws generated in production and handling, resulting in a much lower practical strength than its theoretical strength [2]. On the other hand, there are numerous benefits of oxide glasses compared with other inorganic materials, including transparency, formability, and low cost [1]. Therefore, the focus must be on improving the limiting factors, namely, low damage resistance and low fracture toughness. This would enable the production of thinner and thereby more environmentally friendly glass as well as safer and more reliable glass products. The damage resistance (as measured through hardness and crack initiation resistance) is typically improved via posttreatment such as thermal tempering or ion exchange, which induces a compressive stress layer on the glass surface [1]. However, the fracture toughness (i.e., the internal resistance for cracks to grow [3]) is not significantly affected by these treatments [4]. An approach to increase fracture toughness is rational composition design to obtain an intrinsically tougher structure with improved ability to resist macroscopic crack growth [5,6]. Alterna-

tively, microstructuring of glasses through liquid-liquid phase separation or partial crystallization has been proposed as a toughening method, but either approach makes it challenging to maintain transparency [7,8].

Ideally, postprocessing and compositional design should be combined such that the chosen postprocessing is performed on an optimized glass composition. An example hereof is high-pressure treatment (e.g., hot compression, where the glass is subjected to an isostatic pressure around the glass transition temperature T_g) of glasses containing atoms that can easily change their coordination number (CN) under pressure, such as Al and B [9,10]. Pressure treatment of glasses has been extensively conducted, and especially treatments at or around T_g can result in permanent changes in the structure and properties of bulk glasses [11]. Hot compression generally results in increased density, Vickers hardness, and elastic moduli, but a decrease in crack initiation resistance [12,13]. In terms of structural changes, B is particularly prone to undergo pressure-driven CN changes, which in some cases even persist upon reannealing of the glass around T_g [14]. Furthermore, x-ray diffraction studies of hot- and cold-compressed silica glass have revealed significant changes in the medium-range order (MRO) glass structure [11].

In recent work, we have shown that hot compression at 2 GPa of a lithium aluminoborate glass increases its fracture toughness by a factor of $\sim$2, resulting in a record high fracture toughness of 1.4 MPa m$^{0.5}$ for a bulk oxide glass [5]. The hot compression treatment also increased the Young's

*mos@bio.aau.dk

modulus and Vickers hardness, thus creating a harder, stiffer, and tougher glass. In the previous study, we also investigated two other glass compositions, namely, a soda-lime-silica (window) glass and a sodium borosilicate glass. These glasses also showed a pressure-induced increase in fracture toughness, Young's modulus, and Vickers hardness, but to a much smaller extent than the lithium aluminoborate glass. We ascribed the large fracture toughness increase for the lithium aluminoborate glass to its high propensity for so-called bond switching events, where the network forming species (Al and B) either change or swap CN, where a swapped CN refers to substitution of one or more of the originally neighboring oxygens with other oxygens (i.e., the CN is preserved) [5]. As the simulations revealed that bond switching events occurred to a larger extent in the densified lithium aluminoborate glass than the other glasses, it undergoes more local deformations before fracturing and therefore has a higher degree of nanoplasticity, resulting in a higher fracture toughness.

Indeed, changes in fracture toughness have usually been ascribed to changes in the short-range order (SRO) glass structure [5,15,16], with little emphasis placed on the effect of MRO changes on fracture toughness [17]. That is, more in-depth structural analyses are needed to understand the origin of the pronounced increase in fracture toughness upon hot compression. In this paper, we investigate the pressure-induced changes in structure and properties of alkali aluminoborate glasses containing either lithium, sodium, or potassium. This includes a thorough SRO and MRO structural analysis of the as-produced and hot-compressed glasses by combining x-ray total scattering experiments with molecular dynamics (MD) simulations to elucidate the structural origin of the increase in fracture toughness. Particularly, we study the effect of the ring structures, i.e., the MRO structural signatures, on the mechanical properties of the glasses.

II. METHODS

A. Sample preparation

Three oxide glasses with compositions (in mol %) $25M_2O$-$20Al_2O_3$-$55B_2O_3$ (M = Li, Na, or K) were prepared by the melt-quenching technique. The three compositions will be referred to as LiAlB, NaAlB, and KAlB, respectively. The following raw materials were used: Li_2CO_3 (Sigma Aldrich, >99.9%), Na_2CO_3 (Honeywell, >99.5%), K_2CO_3 (Honeywell, >99.5%), Al_2O_3 (Sigma Aldrich, >99.5%), and H_3BO_3 (Honeywell, >99.5%). These were first mixed according to the composition and then melted in a Pt-Rh crucible in an electric furnace (Entech, Ängelholm, Sweden) at 1400 °C for ~2 h, followed by quenching onto a brass plate. All samples were annealed at their measured glass transition temperature (T_g) for ~30 min. The weight loss from all melts did not exceed 3%.

After annealing, the glass samples were cut into beams and subjected to an isostatic N_2-mediated pressure treatment at 1 and 2 GPa, at the respective T_g, as described in detail elsewhere [5,18]. All lithium aluminoborate glass samples were confirmed to be noncrystalline by powder x-ray diffraction analysis (PANalytical, Empyrean XRD), as shown in Fig. S1 in the Supplemental Material [19]. These measurements were performed on samples crushed in a mortar and transferred to a

zero-background plate of monocrystalline silicon. The diffraction patterns were measured in a θ-θ geometry with a Cu Kα_1 source ($\lambda = 1.54098$ Å) in the range of $2\theta = 5°$–$70°$. We note that the sodium and potassium aluminoborate samples also showed no signs of crystallization during melt quenching based on the x-ray total scattering data.

B. Elastic properties and density

The density ρ of all samples was determined by Archimedes' principle of buoyancy and measured in absolute ethanol ($\geqslant$99.99%) at room temperature. From the density, the atomic packing density C_g was calculated as

$$C_g = \frac{\rho \sum_i f_i \frac{4}{3}\pi N_A \left(xr_A^3 + yr_B^3\right)}{\sum_i f_i M_i}, \quad (1)$$

where f is the molar fraction of component i with the formula A_xB_y, N_A is Avogadro's number, r is the ionic radius, and M is the molar mass. As the ionic radii depend on CNs, we assumed sixfold coordination for the alkali modifiers, twofold coordination for oxygen, and three- to sixfold coordination for B and Al based on existing nuclear magnetic resonance (NMR) spectroscopy data [10,20,21]. We used the ionic radii proposed by Shannon [22]. We note that NMR data were not available for the 2-GPa compressed NaAlB sample nor for the 1- and 2-GPa compressed KAlB samples. As an approximation, we therefore used the data for 1-GPa compressed NaAlB and as-made KAlB samples, respectively.

The elastic properties were determined by ultrasonic echography. The longitudinal V_L and transverse V_T wave velocities were estimated by the pulse-echo method, where sound waves were generated by 10 MHz piezoelectric transducers. Young's Modulus E, Poisson's ratio ν, and shear modulus G were then calculated as

$$E = \rho \frac{3V_L^2 - 4V_T^2}{\left(\frac{V_L}{V_T}\right)^2 - 1}, \quad (2)$$

$$\nu = \frac{E}{2\rho V_T^2} - 1, \quad (3)$$

$$G = \frac{E}{2(1 + \nu)}. \quad (4)$$

C. Fracture toughness

Fracture toughness K_{Ic}, i.e., the critical stress intensity factor for mode I fracture, was measured using the single-edge precracked beam (SEPB) method, following the ASTM standard for ceramics [23] and recent literature for glasses [5,24,25]. We note that the fracture toughness of the 2-GPa compressed glasses was measured using an adapted SEPB method [5,24] due to the smaller sample size which is a result of the limited space within the high-temperature pressure chamber. The glass samples were cut and then ground and polished in ethanol on SiC papers into beams with dimensions of $B \times W \times L = 3 \times 4 \times 25$ mm³ for as-made and 1-GPa compressed samples and dimensions of $1.4 \times 1.9 \times 10$ mm³ for the 2-GPa compressed samples, as described in detail elsewhere [5]. We note that this small beam size does not affect the fracture toughness measurement [5].

Each beam was subjected to Vickers indentation (load = 9.81 N, dwell time = 5 s) on the narrow side (B = 1.4 or 3 mm), where a line of indents was produced with an indent separation of 100 μm. A precrack with a length of ∼0.5×W was then formed in each beam by bridge compression [25], using a groove size of 4 or 6 mm for small and large beams, respectively, and a cross-head speed of 0.05 mm min^{-1}. Each precracked beam was fractured by three-point bending using a cross-head speed of 15 μm s^{-1}, immediately after precrack formation to avoid humidity effects [25]. Finally, K_{Ic} was calculated using the precrack length (measured by 200× magnification microscope) and the measured peak load from the three-point bending experiments. We also calculated the fracture energy based on the values of K_{Ic}, ν, and E [5,23,25,26]. Further details can be found in Refs. [5,25]. Examples of the recorded load-displacement curves are shown in Fig. S2 in the Supplemental Material [19].

D. X-ray total scattering

To understand the structural changes at both SRO and MRO length scales due to both composition variation and densification, we collected x-ray total scattering data at the I15-1 beamline at the Diamond Light Source (λ = 0.161669 Å, E = 76.69 keV). The as-made and hot-compressed glass samples were crushed using an agate mortar, loaded into 1-mm Kapton tubes, held in place by quartz wool, and finally sealed using super glue. Data of an empty capillary and the samples were acquired in the scattering vector range of $Q \sim 0.7$–25 Å^{-1} in scans of 20 min each. The container measurement was subtracted, and Compton and absorption corrections were subsequently applied using the GudrunX software before transforming the structure factor $S(Q)$ to the pair distribution function [in this case the differential correlation function $D(r)$] [27]. We note that the GudrunX program employs the Hannon, Howells, Soper (HHS) functions as described in Ref. [28] as well as a revised Lorch function for the conversion from reciprocal to real space. We refer to the GudrunX manual for a detailed introduction to this procedure [29]. Lastly, $S(Q)$ was converted into the intermediate scattering function $F(Q)$ by

$$F(Q) = [S(Q) - 1]Q. \tag{5}$$

E. MD simulations

The three glass compositions from the experiments, i.e., 25M_2O-20Al$_2$O$_3$-55B$_2$O$_3$ (M = Li, Na, or K), were simulated using classical MD simulations with a GPU-accelerated [30] version of LAMMPS [31]. Based on the recently parameterized SHIK force field suitable for glasses containing Al$_2$O$_3$ and B$_2$O$_3$ [32], we prepared the glasses with varying pressure treatments (0, 1, and 2 GPa), ultimately mimicking the experimental procedure described above. First, 10 000 atoms were randomly placed in a cubic simulation box with side lengths corresponding to the experimentally measured density of the 0-GPa samples described above, while avoiding any unrealistic overlap of atoms. This was followed by an energy minimization and initial mixing of the structures at 2500 K in the NVT ensemble for 100 ps. Next, the sample was mixed for another 700 ps in the NPT ensemble at 2500 K at 0.1, 1.0, and 2.0 GPa, respectively. This step was followed by

quenching the structures to 300 K at 1 K ps^{-1} in the NPT ensemble. During cooling, the pressure was linearly released from 0.1 to 0.0 GPa for the 0-GPa sample, while the remaining samples were maintained at their designated pressures. Next, when reaching 300 K, all structures were subjected to 100 ps of relaxation in the NPT ensemble at 300 K and their designated pressures, followed by another 100 ps in the NPT ensemble at 300 K and zero pressure. This was found to be adequate for ensuring convergence of energy and volume. Finally, the simulated glass structures were recorded for another 100 ps in the NVT ensemble for statistical averaging (sampling every 1 ps). Six independent samples were quenched for each composition, and all shown simulation results are therefore averages of six independent structures for each pressure. We also checked the finite size effect by investigating the structure of four additional simulated glasses with sizes of 0.5×0.5×0.5, 0.75×0.75×0.75, 2×2×2, and 3×3×3 relative to the original box side length, corresponding to system sizes of 1250, 4220, 80 000, and 270 000 atoms, respectively. As seen from the results in Fig. S3 in the Supplemental Material [19], the use of 10 000 atoms in this paper is sufficient to avoid finite size effects.

Now the $S(Q)$ and $D(r)$ functions were computed for all simulated samples using the R.I.N.G.S. software [33,34]. The computed $D(r)$ was broadened by convoluting the $D(r)$ with a Gaussian distribution with a full width at half maximum (FWHM) of

$$\text{FWHM} = \frac{5.437}{Q_{max}}, \tag{6}$$

where Q_{max} is the maximum wave vector used in the diffraction experiment (25 Å^{-1}).

We also calculated the ring size distribution using the R.I.N.G.S. software [33,34]. This was only done for the NaAlB glass since this composition showed the best agreement between experimental and simulated $S(Q)$. Three ring definitions were used (King's, Guttman's, and primitive rings), and the searches were conducted to a ring size up to n = 14, with n allowed to be both Al and B atoms.

III. RESULTS AND DISCUSSION

A. Medium-range structure

Figure 1(a) shows the total scattering structure factors [$S(Q)$] determined from experiments for all the as-made and densified glasses. Comparisons between the experiments and simulations are shown in Fig. 1(b) for the as-made glasses, while Figs. S4(a)–S4(d) in the Supplemental Material [19] show the comparison for the hot-compressed glass samples as well as the curves covering the full Q range. To assist the interpretation, simulated x-ray weighted partial structures factors [$S_{ij}(Q)$] are shown in Fig. S5 in the Supplemental Material [19]. While it is not straightforward to correlate $S(Q)$ to structural features, it is well recognized that the low-Q region [including the first sharp diffraction peak (FSDP)] describes the MRO structure of the glass, as it relates to the size and geometry of the cage or ringlike structures [35–37]. The second peak, also known as the principal peak (PP), is commonly ascribed to the size of the geometric structure (e.g., tetrahedron) created by the network formers in the glass (here,
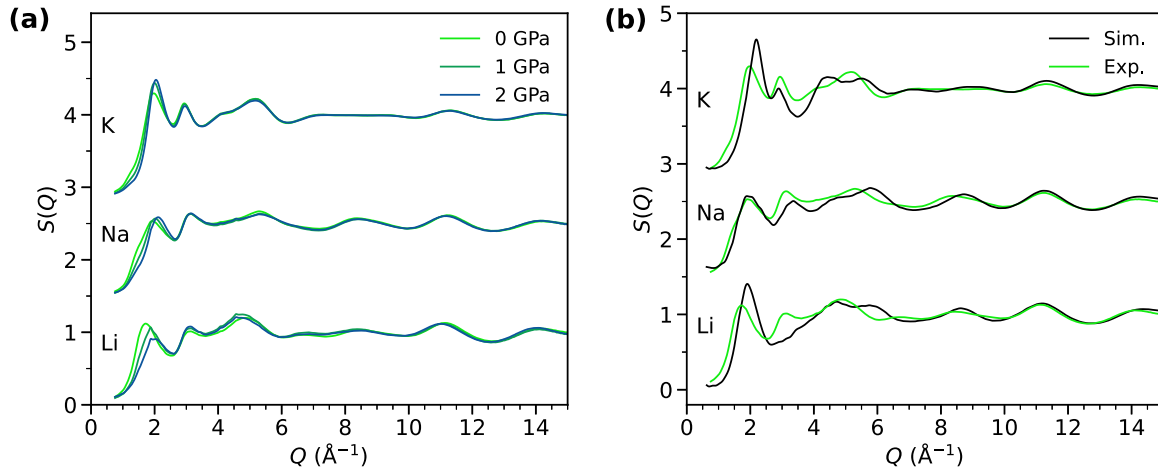
FIG. 1. X-ray structure factor $S(Q)$ for the lithium, sodium, and potassium aluminoborate glasses. (a) Experimental data for as-made and hot-compressed samples. (b) Comparison of experimental and simulated $S(Q)$ for the as-made (0 GPa) samples. For clarity, the Na and K spectra are offset by $+1.5$ and $+3.0$, respectively.

Al and B). The oscillations at higher Q values describe the SRO structure [36]. For comparison, $S(Q)$ curves are plotted alongside the real-space differential correlation function $D(r)$ in Q space in Fig. S6 in the Supplemental Material [19].

As shown in Fig. 1(a), the MRO clearly varies with pressure, both in terms of the FSDP position and intensity. Such changes upon compression treatment have been observed previously for other glass compositions [14,38–40]. An increasing FSDP position can be interpreted as a contraction of the cagelike structures in the glass network [35,40], which is supported by the increasing density that is also observed in the pressure-treated glasses (see Sec. III C) [35,40]. Alternatively, it can be interpreted as a decrease in the average ring size, where the ring size refers to the number of atoms included in each chemically bonded ring [41]. The FSDP intensity decreases with increasing pressure for the LiAlB glass, which matches most observations in the literature on other densified glasses [35,40]. On the other hand, both NaAlB and KAlB glasses exhibit an increase in peak intensity with increasing pressure. The FSDP intensity has previously been ascribed to the concentration of interstitial voids in the glass structure [35,37], but the intensity is generally difficult to interpret due to its correlation with the scattering-length-dependent partial structure factors. Finally, the FSDP area, as determined by integrating to the first $S(Q)$ minima, decreases with pressure for the LiAlB and NaAlB glasses, with LiAlB showing the largest decrease, whereas the KAlB glass shows only a small increase (Fig. S7(a) in the Supplemental Material [19]).

We note that, in some cases, it can be challenging to interpret the x-ray $S(Q)$ FSDP area, as it may be difficult to separate the FSDP from the PP (i.e., the peak at the second lowest Q). In these cases, it can be more straightforward to interpret data which are weighted differently, e.g., neutron $S(Q)$, or the neutron or x-ray interference function $F(Q)$ [Eq. (5)], which is like the $S(Q)$ function but with higher weight on the high-Q region [36]. Changing from x-ray to neutron weighting requires partial $S_{ij}(Q)$ data, which has not been possible to obtain experimentally herein. Therefore, the experimental data have been evaluated by calculating the $F(Q)$ FSDP area (again by integrating to the first minima) to compare the trends

in $F(Q)$ vs $S(Q)$ FSDP area, as shown in Fig. S7(b) in the Supplemental Material [19]. The two areas feature different values as the weighting is different, but most importantly, the trends are similar. As such, we will continue to use the experimental data based on x-ray $S(Q)$ in the following.

Comparing the experimental and MD-simulated $S(Q)$ [Fig. 1(b)], the higher-Q range (SRO structure) is described well by the used SHIK potential, whereas the lower-Q range (MRO structure) is not as well described. Considering the FSDP, the peak position and intensity agree well among experiments and simulations for the NaAlB glass, whereas both the peak position and intensity are different for the KAlB and LiAlB glasses. The trend of increasing FSDP position upon hot compression is well described for all glasses, although the absolute values are only well captured for the NaAlB glass (Fig. S7(c) in the Supplemental Material [19]). Moreover, considering the changes in the FSDP area with pressure, this trend is also well described by the simulations, although the absolute values are not replicated (Fig. S7(a) in the Supplemental Material [19]).

Contrary to the experimental data, we have access to the partial $S_{ij}(Q)$ from the simulations, enabling a comparison of the differently weighted $S(Q)$ data to conclude whether a change in weighting gives a clearer separation of FSDP and PP and a change in the trends of the FSDP area and position. To this end, we have calculated $S(Q)$ from the partials by weighting with atomic number (x-ray), coherent scattering lengths (b_c neutron, taken from Ref. [42]), and with equal weighting of all atoms. The three $S(Q)$'s for each of the as-made samples are shown in Fig. S8 in the Supplemental Material [19], revealing that only the LiAlB glass features a clearer separation of FSDP and PP when using neutron weighting, whereas the NaAlB and KAlB glasses both show the clearest separation for the x-ray $S(Q)$. Furthermore, the changes in the FSDP position and area with pressure for both the experimental and differently weighted simulated $S(Q)$ data are shown in Figs. S9(a)–S9(c) and S9(d)–S9(f), respectively, in the Supplemental Material [19]. For the FSDP position, the same trend is observed independent of weighting, with only minor changes in the absolute values. For the FSDP
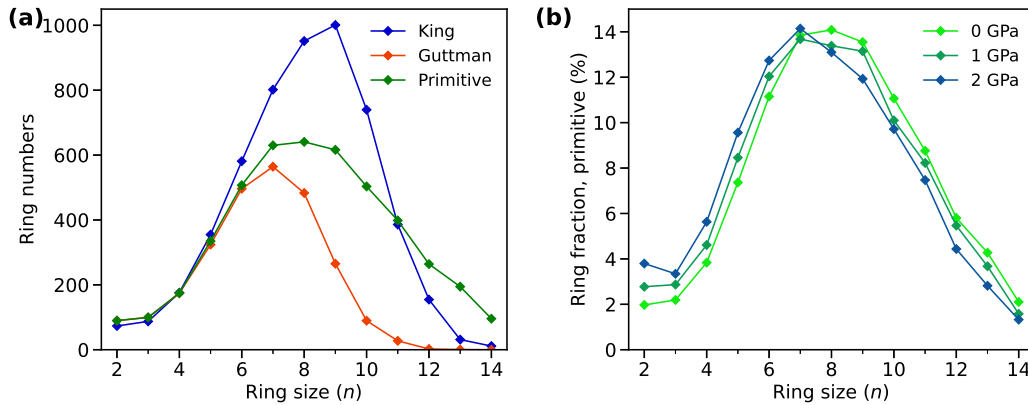
FIG. 2. Ring size distribution for (a) as-made NaAlB glass using Guttman's, King's, and primitive ring definitions and (b) both as-made and compressed NaAlB glasses using the primitive rings definition.

area, the same is valid for the LiAlB glass, whereas the NaAlB and KAlB glasses both feature a slightly increasing negative trend when changing to neutron weighted data, with the most pronounced change for the KAlB glass. Even though the trends in the FSDP area with pressure become more similar for the three glasses when changing to neutron weighting, we still find no universal relation to describe all the samples.

The above comparison for experimental and simulated data shows that the NaAlB glass composition is best described by the SHIK potential. This is most likely because the SHIK potential was first optimized for various silicate and aluminosilicate glasses, including a sodium aluminosilicate composition [43]. This parameterization showed that short-range interaction parameters were unnecessary for the Na-Al and Al-Si atom pairs, enabling easy transferability to other alkali aluminosilicate glasses. Furthermore, when the potential was expanded to include boron, only alkali borate glass compositions were used for the optimization since the short-range interaction parameters for the Al-B atom pair were also redundant [32]. Based on the results presented herein, it could appear that some force field optimization would be beneficial for the K and Li parameters. Such an optimization is beyond the scope of this paper, and we therefore mainly focus on the NaAlB glass in the following, as it shows the best agreement with experimental data.

Based on the observed changes in FSDP, the hot compression treatment can cause changes in the MRO structure of the glasses. To study this further, the ring size distributions have been analyzed based on the MD-simulated structures. For the reasons mentioned above, we only analyze the NaAlB glasses using the R.I.N.G.S. software [33,34]. The aim is to elucidate the pressure-induced changes in the ring-type structural units embedded in the network structure. R.I.N.G.S. computes ring-type structures from three definitions, namely, Guttman's, King's, and primitive. The obtained ring size distributions are shown in Figs. 2 and S10 in the Supplemental Material [19]. The total number of rings found for each definition can be seen in Table SI in the Supplemental Material [19]. Detailed descriptions of all three definitions can be found in Refs. [33,34].

The ring size distributions reveal that the three definitions find almost the same number of small-sized rings ($n \leqslant 5$), whereas a considerable variation is observed in the total

number of large rings ($n > 5$) and the distribution of these, like what has previously been found for silica glasses [41]. The ring size distribution using the primitive rings definition agrees well with previous results for similar compositions [44]. Previous studies have often used the primitive rings definition for this analysis [44–48], although no argument for this is typically provided, while the Guttman's and King's definitions are rarely used [41,49,50]. Here, the calculated ring size distributions reveal a pressure-induced decrease in the number of larger-sized rings ($n > 8$, $n > 6$, and $n > 7$ for King's, Guttman's, and primitive rings definitions, respectively) and an increase in the number of smaller-sized rings ($n \leqslant 8$, $n \leqslant 6$, and $n \leqslant 7$ for King's, Guttman's, and primitive rings definition, respectively). We find only a small number of $n = 3$ rings, which would include superstructural borate units such as the boroxol rings. Boroxol rings are characteristic for borate glasses with trigonal boron atoms based on experimental Raman and NMR spectroscopy data [51–54]. Previous Raman spectroscopy studies on the alkali aluminoborate glasses show that these superstructural borate units, also including di- and triborates, are indeed present in these glasses [10,55]. From the ring size distribution, it is evident that the superstructural borate units are poorly described by the MD simulations, which is known to be a general issue for classical MD simulations [44,56,57].

Furthermore, we find that the ring size distribution shifts toward smaller rings upon hot compression, lowering the average primitive ring size from 8.2 to 7.6, in agreement with the shift in the FSDP position. To further correlate the FSDP position to the ring size, we use the following definition from crystallography:

$$Q = \frac{2\pi}{d}, \tag{7}$$

where d is the distance between planes in crystalline materials. For glasses, we may regard d as the average ring diameter, as these may form pseudoplanes, giving rise to diffraction [58]. The main part of the ring structures in the glass will be elliptical-like structures, having both a small and large diameter (see Fig. S11(b) in the Supplemental Material [19]). Here, we use the small diameter to analyze whether the pseudoplanes found from the simulations (i.e., the rings) correspond to the MRO structures that give rise to FSDP.
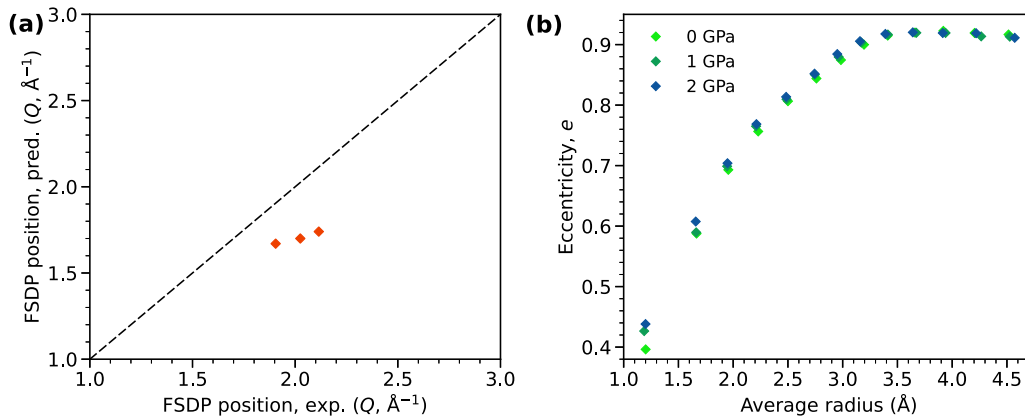
FIG. 3. (a) Predicted first sharp diffraction peak (FSDP) position using the small ring diameter as a function of the experimentally determined FSDP position for the as-made and hot-compressed NaAlB glasses. The dashed line is a guide for the eye, representing one-to-one agreement. (b) Ring eccentricity as a function of average radius of the rings found using the primitive rings definition for the simulated NaAlB glasses, prepared at 0, 1, and 2 GPa.

This diameter is corrected with the fraction of each ring size, resulting in an average diameter of the three NaAlB glasses to be 3.77, 3.69, and 3.61 for 0-, 1-, and 2-GPa samples, respectively. This converts into Q values of 1.67, 1.70, and 1.74 Å^{-1}, respectively. These values generally match the experimental FSDP positions (see Fig. S7(c) in the Supplemental Material [19]). The trend of increasing FSDP position with increasing pressure is also reproduced, as shown in Fig. 3(a).

While ring size distribution analysis is a straightforward approach to characterize differences in the MRO structures, it only counts the number of atoms in the rings, neglecting details about the ring shapes. In the following, we also study the geometry of the rings by defining some geometric measures for characterizing the rings. Specifically, we have calculated the ring center area, the deviation of the rings from planarity (planeness), and the ring eccentricity (a measure of the circularity of an ellipsoid, with a circle having an eccentricity of 0). These concepts are described in detail in Note 1 in the Supplemental Material [19]. Again, these calculations are only performed for the NaAlB glass, as these glass structures are best reproduced by the used force field. The results of these additional ring analyses are shown in Figs. 3(b) and S12 in the Supplemental Material [19] for the as-made and hot-compressed NaAlB glasses. The calculations were done based on all three ring definitions, but as the difference in the results between each definition was minimal, we only show here the results based on the primitive rings definition. First, we find only minor changes in the ring center area with pressure and only for the very large ring structures ($n > 10$), whereas the remaining rings exhibit approximately constant area (Fig. S12(a) in the Supplemental Material [19]). Second, the planeness analysis reveals that the smaller rings ($n < 7$) become less planar with pressure, while the larger rings ($n > 7$) become more planar with pressure (Fig. S12(b) in the Supplemental Material [19]). Third, the ring eccentricity is calculated using two different approaches based on how the small and large radii are found in the ring structures (see Note 1 in the Supplemental Material [19]), as shown in Figs. 3(b) and S12(c) in the Supplemental Material [19], respectively. Both analyses reveal that the eccentricity increases slightly upon

compression, suggesting that rings become more elliptical for almost all ring sizes, accompanied by a decrease in the average ring radius. As such, this analysis shows small changes in the ring topology with pressure, although these changes do not appear to affect the center area of the rings, as have often been connected to the changes in FSDP.

B. Short-range structure

As evident from Fig. 1(a), hot compression appears to also cause some changes in the SRO with the largest changes observed for the LiAlB glass. Previously, changes in the SRO structure have been used to explain the pressure-induced changes in the properties of compressed aluminoborate glasses [5,10]. We also observe changes in the $S(Q)$ PP for all glasses upon compression, which is likely attributed to changes in B and Al CNs (i.e., the transformation of B^{III} into B^{IV} and Al^{IV} into Al^{V} and Al^{VI}, respectively), as observed from solid-state NMR experiments in previous work [10,20,21].

Here, $S(Q)$ can be transformed into the pair distribution function [in this case, the differential correlation function $D(r)$], for which the peaks are a measure of the probability of finding two atoms within a given distance (r) in the glass. Figure 4(a) shows the experimental $D(r)$ curves with various peaks that are associated with different atom-atom correlations, as assigned based on the partial $d(r)$ obtained from MD simulations. Specifically, we find seven distinct peaks for $r < 5\,\text{Å}$, where the first four peaks can be assigned, as shown in the figure. Only selected atom-atom correlations are shown here, while all partial $d(r)$ contributions are shown in Fig. S13 in the Supplemental Material [19]. The peak positions are listed in Table SII in the Supplemental Material [19] for both experimental and simulated $D(r)$. The assigned peak positions agree well with those reported in the literature in terms of atomic distances [32,46,59].

A comparison of the experimental and MD-simulated $D(r)$ is shown in Fig. 4(b) for the as-made samples (see Figs. S14(a) and S14(b) in the Supplemental Material [19] for comparisons of the hot-compressed samples). The simulated $D(r)$ provides
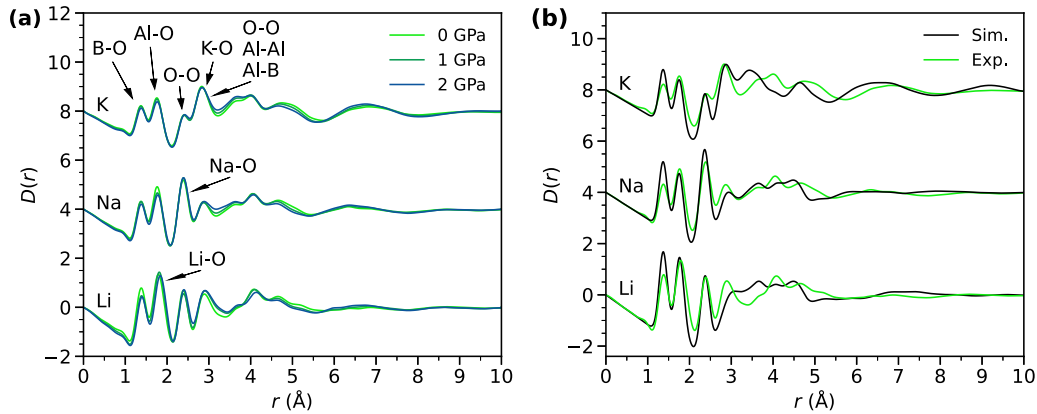
FIG. 4. Differential correlation function $D(r)$ calculated from the experimental x-ray structure factor $S(Q)$. (a) Experimental data for as-made and hot-compressed samples, including peak assignments. Assignments shown for the top curve are also valid for the two lower curves, except the alkali-oxygen assignment. (b) Comparison of experimental and molecular dynamics (MD)-simulated $D(r)$ for the as-made samples. For clarity, the Na and K spectra are offset by +4 and +8, respectively.

a good representation of the first four peaks of the experimental $D(r)$, whereas the peaks at r values above ~ 3 Å differ slightly, especially for the LiAlB and KAlB compositions. This agrees with the $S(Q)$ comparison in Sec. III A, where the best agreement between experimental and simulated data was found at high Q values and for the NaAlB composition.

Interestingly, the bond lengths increase slightly upon hot compression, which is seen as increased peak positions with increasing pressure of the first four peaks in both the experimental and simulated $D(r)$. This is visualized for the first peak in Fig. S14(c) in the Supplemental Material [19]. We attribute this to the increase in the Al and B CNs (i.e., B^{III} to B^{IV} and Al^{IV} to Al^{V} and Al^{VI}), as shown in Table I, where the CN data are taken from previous NMR experiments [10,20,21]. That is, the oxygen atoms are pushed further away from the Al/B atom when an additional oxygen must be accommodated in the first coordination sphere. However, increased bond lengths

TABLE I. CN distributions for B and Al from both previous NMR experiments and the present MD simulations. NMR data were not available for the 2-GPa compressed NaAlB sample and the 1- and 2-GPa compressed KAlB samples. The suffixes of the glass sample names are based on the used pressure during hot compression, i.e., 0 for the as-made glass, and 1 and 2 for the 1- and 2-GPa compressed glasses, respectively.

Glass sample	B^{III}/B^{IV} (%)	Avg. B (NMR)	Avg. B (sim)	$Al^{IV}/Al^{V}/Al^{VI}$ (%)	Avg. Al (NMR)	Avg. Al (sim)
LiAlB-0[a]	83.4/16.6	3.17	3.14	74/23/3	4.29	4.08
LiAlB-1[a]	76.4/23.6	3.24	3.23	49/39/12	4.63	4.19
LiAlB-2[a]	70.3/29.7	3.30	3.33	34/47/19	4.85	4.37
NaAlB-0[b]	86/14	3.14	3.11	96/4/0	4.04	4.01
NaAlB-1[b]	82/18	3.18	3.18	88/9/3	4.15	4.03
NaAlB-2	–	–	3.24	–	–	4.07
KAlB-0[c]	94/6	3.06	3.13	95/4/1	4.06	4.01
KAlB-1	–	–	3.17	–	–	4.02
KAlB-2	–	–	3.23	–	–	4.04

[a]Experimental CNs taken from Ref. [10].
[b]Experimental CNs taken from Ref. [21].
[c]Experimental CNs taken from Ref. [20].

have also been observed for compressed silica glass, where there is no observed change in the Si CN [11]. The changes in silica glass have previously been ascribed to a broader bond angle distribution and the Si-O bond becoming less covalentlike [60]. This indicates that increased CNs are likely not the sole reason for the increased bond lengths in the aluminoborate glasses. Furthermore, we note that the M-O bond lengths ($M =$ Li, Na, or K) also increase with pressure, as seen from the increase in the position of the peaks assigned to these bonds, but also from the partial $d(r)$ where the first peak of the Li-O and Na-O partials increase in position with pressure, while it remains constant for K-O. This contrasts with the previous ^{23}Na MAS NMR results that suggest a decrease in alkali-oxygen bond lengths with increasing pressure [61].

Although the peak positions align well for the experimental and simulated $D(r)$, the intensities and peak areas are not fully replicated, indicating small differences in the experimental and simulated CNs. However, as many variables are involved in the calculation of $D(r)$, including broadening functions, it is difficult to directly compare the intensities and peak areas from the simulations and experiments. A better comparison is to consider the CNs. As many of the studied compositions have already been probed by NMR in the literature [10,20,21], here, we compare the Al and B CNs from NMR and the present MD simulations (Table I). We find that the average B CN is well replicated in the simulations, while the average Al CN is slightly underestimated, particularly for the LiAlB sample. Such small differences are expected due to the much higher cooling rates used in the simulations than the experiments.

C. Mechanical properties

The pressure-induced structural changes that are described above affect the mechanical properties of the glasses. As shown in Table II, all three glass compositions show an increase in ρ, G, and E, and they all show a small decrease in ν with increasing pressure, in agreement with previous findings [5,20,62]. A more densely packed system with higher average CN has more atomic constraints per unit volume, leading to an increased E [63]. The largest increase in ρ is seen for the

TABLE II. Density (ρ), packing density (C_g), fracture toughness (K_{Ic}), shear modulus (G), Young's modulus (E), and Poisson ratio (ν). Estimated errors do not exceed 0.01 g cm^{-3}, 0.05 MPa m$^{0.5}$, 0.5 GPa, 1 GPa, and 0.005 for ρ, K_{Ic}, G, E, and ν, respectively. Data for the LiAlB glass are reproduced from Ref. [5]. The suffixes of the glass sample names are based on the used pressure during hot compression, i.e., 0 for the as-made glass, and then 1 and 2 for the 1- and 2-GPa compressed glasses, respectively. We note that the present ρ data are all within 0.05 g cm^{-3} ($< 2\%$ of change) of previous reports on similar glass compositions [5,9,10,20].

Glass sample	ρ (g cm^{-3})	C_g (—)	K_{Ic} (MPa m$^{0.5}$)	G (GPa)	E (GPa)	ν (—)
LiAlB-0	2.238	0.546	0.69	26	67	0.279
LiAlB-1	2.420	0.591	1.13	35	90	0.271
LiAlB-2	2.596	0.635	1.36	46	115	0.262
NaAlB-0	2.255	0.514	0.71	17	44	0.291
NaAlB-1	2.359	0.538	0.83	21	55	0.286
NaAlB-2	2.471	0.564	1.07	26	65	0.274
KAlB-0	2.175	0.500	0.59	11	28	0.303
KAlB-1	2.285	0.525	0.64	15	38	0.296
KAlB-2	2.417	0.555	0.87	19	49	0.283

LiAlB and NaAlB glasses, which contain the smallest modifier ions, giving the ability to a more densely packed structure, as is also seen from the increase in C_g. The largest increase in E is found for the LiAlB glass, indicating a larger increase in the connectivity and atomic constraints of this glass upon hot compression than the two other glasses [64]. This is also supported by the previously determined CNs (Table I), i.e., the LiAlB samples contain the largest fraction of Al and B species with higher CNs in both the as-made and compressed glasses compared with the two other compositions. Interestingly, the pressure treatment causes a larger increase in G than E for the LiAlB and NaAlB glasses, with a difference in the increase of 5% for both samples. This is opposite to findings in previous studies where E and G either increase similarly upon pressure treatment or where E increases more than G [11,62,65]. Both E and G are related to the bond energies, atomic constraints of the bonds, and C_g [66]. According to the

theoretical calculations of E and G in Ref. [66], E is influenced mostly by changes in C_g, while the other parameters are found to influence the two moduli equally.

Now instead of focusing only on the equilibrium mechanics, we will focus on the fracture toughness of the glasses. Figure 5(a) shows that the hot-compression posttreatment causes a large increase in K_{Ic} for all three glass compositions, with the most pronounced increase observed when the pressure increases from 0 to 1 GPa for the LiAlB glass. To reveal the structural origin of this toughening, we first attempt to predict K_{Ic} using Rouxel's fracture toughness model [67]. Here, the theoretical fracture surface energy is predicted based on the nominal glass composition, using the experimental ρ, E, ν, the molar mass of the glass, and the bond energies of the cation-oxygen bonds contained in the glass, with the assumption that the crack only propagates through one bond in each LiO$_x$, AlO$_x$, and BO$_x$ oxide unit [5]. Then K_{Ic} is calculated as

$$K_{Ic} = \sqrt{\frac{2\gamma E}{1 - \nu^2}}, \tag{8}$$

where E and ν are taken as the experimental values, while γ is the theoretical fracture surface energy. This model assumes no plastic deformation during fracture, which is usually a reasonable assumption for oxide glasses. Here, we find that this model provides a reasonable prediction of the experimental K_{Ic} values [Fig. 5(b)] [5], although with a slight underestimation of most values, with the 2-GPa compressed glasses showing the largest difference. From Rouxel's model, it is evident that the changes in ρ, E, and ν with pressure contribute to the increase in K_{Ic} with pressure. This is also reflected in the approximate linear relationships between K_{Ic} and E or C_g (Figs. S15(a) and S15(b) in the Supplemental Material [19]). Here, K_{Ic} is, as seen from Eq. (8), positively correlated with E, where E is determined by both the number of bonds per unit volume and the bond energies [63], and these bonds must be broken for the crack to propagate [15,67]. Therefore, K_{Ic} is also correlated to the average CN of the network-forming species in the glass, as increased CNs lead to increased number of atomic constraints per unit volume and hence an increased E.
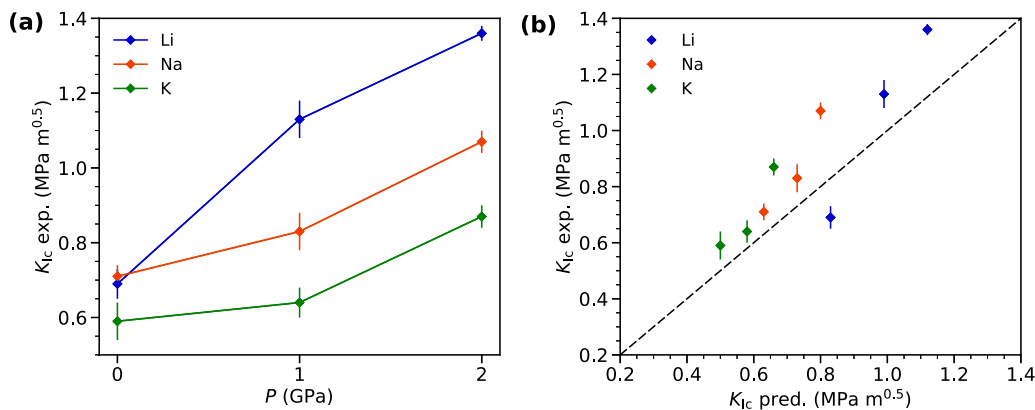

FIG. 5. (a) Pressure dependence of the experimental determined fracture toughness (K_{Ic}) values. (b) Comparison of experimental K_{Ic} and predicted K_{Ic}. Experimental and predicted K_{Ic} data for LiAlB glasses are reproduced from Ref. [5]. The dashed line in (b) represents the one-to-one correlation.
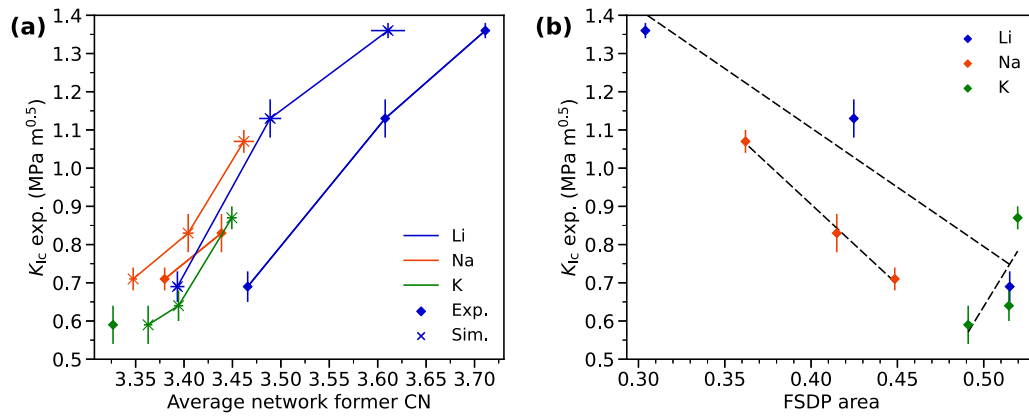
FIG. 6. Correlation between experimental fracture toughness (K_{Ic}) and (a) average coordination number (CN) of network forming species (Al and B) as obtained from experiments and simulations, and (b) area of the first sharp diffraction peak (FSDP), obtained from experimental x-ray $S(Q)$. Dashed lines in (b) are linear fits to data for each glass composition. Data for LiAlB glass have previously been published in Ref. [5]. Experimental CNs are taken from Refs. [10,20,21].

The correlation between K_{Ic} and the average CN of the network-forming species (Al and B) is analyzed in Fig. 6(a), showing a clear, positive correlation. Experimental CN values based on NMR data in the literature are not available for some samples. Because the experimental x-ray $D(r)$ intensity is strongly correlated with the scattering length dependent partial structure factors and due to significant overlap of partials, the CNs cannot be determined from the x-ray data. Therefore, the simulated CN values are also included in this figure, which show the same trend. This shows that increasing the fractions of higher-coordinated network-forming species in the glass will result in a glass with a higher K_{Ic}. However, this is only valid when studying the same glass composition, as the 0- and 1-GPa NaAlB samples show a higher K_{Ic} than the 0-GPa LiAlB sample, although the LiAlB sample has a higher average CN value.

To further investigate which structural features are responsible for the increase in K_{Ic}, the correlation between K_{Ic} and the FSDP area is shown in Fig. 6(b), and the correlation between K_{Ic} and the FSDP position is shown in Fig. S15(c) in the Supplemental Material [19]. Like the correlation in Fig. 6(a), Fig. 6(b) shows an almost linear correlation between K_{Ic} and the FSDP area for each glass composition. However, there is no master curve describing the behavior of all samples. The same is the case for the correlation between K_{Ic} and the FSDP position. We have also compared the correlation shown in Fig. 6(b) with the correlation between K_{Ic} and the FSDP area as derived from $F(Q)$. As shown in Fig. S15(d) in the Supplemental Material [19], we find the same trend with both scattering functions. The KAlB glass shows a positive correlation, opposite the LiAlB and NaAlB samples, which is likely explained by the partial $S_{ij}(Q)$ (see Fig. S5 in the Supplemental Material [19]). That is, the K-containing atom pairs all contribute to FSDP, while the Li- and Na-containing atom pairs have little to no contribution to FSDP.

D. Structural origin of increase in fracture toughness

Considering the above-presented results, it is evident that the pressure treatment causes an increase in K_{Ic}, increase in the CN of the network-forming species, and changes in the

topology of the ring structures, including a decrease in the average ring size and a change toward more elliptical small rings. As such, in addition to the SRO changes, we observe systematic pressure-induced changes in the MRO structure, as seen from the changes in FSDP position and area. This suggests that the increase in K_{Ic} cannot be linked to a single structural event but is influenced by multiple changes in both SRO and MRO structure. Previously, we attributed the large increase in K_{Ic} for the LiAlB glass to the higher propensity for bond switching events, i.e., SRO structural rearrangement that results in increased plasticity of the glass [5]. Increasing plasticity is thereby caused by the adaptability of the network, as a more adaptable network will be more prone to initiate structural changes before bond breaking during a fracture event. Consequently, it appears likely that, when the number of structural changes upon hot compression increases, the adaptability of the structural network is higher. This plasticity or adaptability increases upon densification, suggesting that the structure allows for atomic rearrangement and hence for the compressed elements to decompress or expand back to the initial uncompressed state before fracturing.

As the SRO structures (e.g., polyhedra) are part of the MRO ring-type structures, the events that occur on the SRO scale (e.g., CN changes) will directly lead to changes in the MRO structures. As stated above, we previously showed high adaptability in the SRO structures of these glasses, and based on this reasoning, the adaptability will also be reflected in the MRO structures. Due to this adaptability, we infer that the observed pressure-induced changes in the ring structures are reversible if the glass is subjected to mechanical stress as in a fracture process. In other words, the energy needed for these glasses to fracture increases as the initial energy will be spent on reversing the compressed SRO and MRO structural units before breaking bonds and eventually fracturing the sample. Furthermore, it is known that the hot-compressed glass has a lower apparent fictive temperature, i.e., lower average potential energy (corresponding to higher bond energy) than an ambient pressure produced glass [14,68,69]. When an external load is applied to the compressed glass, the local relaxation from higher to lower bond energy will be triggered before fracturing, and this balances some of the

external energy, leading to an increase of fracture toughness [5]. This is consistent with the revealed structural origin of the increase of fracture toughness in aluminoborate glasses upon hot-compression treatment. These observations suggest an even larger plasticity effect than the previously reported bond switching analysis [5], which is also in agreement with the observed difference between predicted and experimental K_{Ic} [Fig. 5(b)].

IV. CONCLUSIONS

We have studied the changes in SRO and MRO structure of hot-compressed alkali aluminoborate glasses and their impact on the hot-compression-induced increase in fracture toughness. Independent of the type of alkali element, the hot-compression treatment causes significant changes to FSDP in the x-ray structure factor, along with an increase in bond lengths, as seen in the differential correlation function. The ring size distribution and ring topology analyses reveal that the changes in MRO originate from a decrease in the average ring size along with the smaller rings becoming more elliptical upon densification. The increase in bond lengths is caused by an increase in the CN of the network-forming species (Al and B). The changes in the ring structures have been correlated to the increased fracture toughness, with good correlation for each composition, indicating that the MRO correlates directly to the fracture toughness. A similar trend is found when correlating the average CN of network-forming species to the fracture toughness. For both correlations, no overall trend for all samples can be observed, indicating that the increase in fracture toughness is influenced by multiple structural events

at different length scales. Indeed, the results for the studied glass compositions suggest that not only stress-induced changes in the SRO structures influence fracture toughness but also changes in the MRO structures. This should be considered in the future design of intrinsically tough oxide glasses.

The data supporting the results within this paper are available from the corresponding author upon request.

[1] L. Wondraczek, J. C. Mauro, J. Eckert, U. Kühn, J. Horbach, J. Deubener, and T. Rouxel, Towards ultrastrong glasses, Adv. Mater. **23**, 4578 (2011).

[2] L. Wondraczek, E. Bouchbinder, A. Ehrlicher, J. C. Mauro, R. Sajzew, and M. M. Smedskjaer, Advancing the mechanical performance of glasses: Perspectives and challenges, Adv. Mater. **34**, 2109029 (2022).

[3] T. Rouxel and S. Yoshida, The fracture toughness of inorganic glasses, J. Am. Ceram. Soc. **100**, 4374 (2017).

[4] A. K. Varshneya, Chemical strengthening of glass: Lessons learned and yet to be learned, Int. J. Appl. Glass Sci. **1**, 131 (2010).

[5] T. To, S. S. Sørensen, J. F. S. Christensen, R. Christensen, L. R. Jensen, M. Bockowski, M. Bauchy, and M. M. Smedskjaer, Bond switching in densified oxide glass enables record-high fracture toughness, ACS Appl. Mater. Interfaces **13**, 17753 (2021).

[6] J. Sehgal and S. Ito, A new low-brittleness glass in the soda-lime-silica glass family, J. Am. Ceram. Soc. **81**, 2485 (1998).

[7] Q. Fu, E. M. Aaldenberg, E. N. Coon, T. M. Gross, A. M. Whittier, B. M. Abel, and D. E. Baker, Tough, bioinspired transparent glass-ceramics, Adv. Eng. Mater. **24**, 2200350 (2022).

[8] J. F. S. Christensen, S. S. Sørensen, T. To, M. Bauchy, and M. M. Smedskjaer, Toughening of soda-lime-silica glass by nanoscale phase separation: Molecular dynamics study, Phys. Rev. Mater. **5**, 093602 (2021).

[9] K. Januchta, R. E. Youngman, A. Goel, M. Bauchy, S. J. Rzoska, M. Bockowski, and M. M. Smedskjaer, Structural origin of high crack resistance in sodium aluminoborate glasses, J. Non-Cryst. Solids **460**, 54 (2017).

[10] K. Januchta, R. E. Youngman, A. Goel, M. Bauchy, S. L. Logunov, S. J. Rzoska, M. Bockowski, L. R. Jensen, and M. M. Smedskjaer, Discovery of ultra-crack-resistant oxide glasses with adaptive networks, Chem. Mater. **29**, 5865 (2017).

[11] M. Guerette, M. R. Ackerson, J. Thomas, F. Yuan, E. B. Watson, D. Walker, and L. Huang, Structure and properties of silica glass densified in cold compression and hot compression, Sci. Rep. **5**, 15343 (2015).

[12] K. G. Aakermann, K. Januchta, J. A. L. Pedersen, M. N. Svenson, S. J. Rzoska, M. Bockowski, J. C. Mauro, M. Guerette, L. Huang, and M. M. Smedskjaer, Indentation deformation mechanism of isostatically compressed mixed alkali aluminosilicate glasses, J. Non-Cryst. Solids **426**, 175 (2015).

[13] S. Striepe, M. M. Smedskjaer, J. Deubener, U. Bauer, H. Behrens, M. Potuzak, R. E. Youngman, J. C. Mauro, and Y. Yue, Elastic and micromechanical properties of isostatically compressed soda-lime-borate glasses, J. Non-Cryst. Solids **364**, 44 (2013).

[14] M. M. Smedskjaer, R. E. Youngman, S. Striepe, M. Potuzak, U. Bauer, J. Deubener, H. Behrens, J. C. Mauro, and Y. Yue, Irreversibility of pressure induced boron speciation change in glass, Sci. Rep. **4**, 3770 (2014).

[15] K. Januchta, P. Liu, S. R. Hansen, T. To, and M. M. Smedskjaer, Indentation cracking and deformation mechanism of sodium aluminoborosilicate glasses, J. Am. Ceram. Soc. **103**, 1656 (2020).

[16] T. To, C. Gamst, M. B. Østergaard, L. R. Jensen, and M. M. Smedskjaer, Fracture energy of high-Poisson's ratio oxide glasses, J. Appl. Phys. **131**, 245105 (2022).

[17] M. Wang, B. Wang, T. K. Bechgaard, J. C. Mauro, S. J. Rzoska, M. Bockowski, M. M. Smedskjaer, and M. Bauchy, Crucial effect of angular flexibility on the fracture toughness and nanoductility of aluminosilicate glasses, J. Non-Cryst. Solids **454**, 46 (2016).

[18] M. M. Smedskjaer, S. J. Rzoska, M. Bockowski, and J. C. Mauro, Mixed alkaline earth effect in the compressibility of aluminosilicate glasses, J. Chem. Phys. **140**, 054511 (2014).

[19] See Supplemental Material at http://link.aps.org/supplemental/10.1103/PhysRevMaterials.7.053607 for further details about structural and mechanical properties of the studied glass samples, including description of the ring topology analysis with additional figures, XRD spectra, load-displacement curves, detailed $S(Q)$ and $D(r)$ comparisons, and partial $S_{ij}(Q)$ and $d(r)$ curves.

[20] K. Januchta, M. Bauchy, R. E. Youngman, S. J. Rzoska, M. Bockowski, and M. M. Smedskjaer, Modifier field strength effects on densification behavior and mechanical properties of alkali aluminoborate glasses, Phys. Rev. Mater. **1**, 063603 (2017).

[21] A. Veber, M. M. Smedskjaer, and D. de Ligny, Relaxation behavior of densified sodium aluminoborate glass, Acta Mater. **198**, 153 (2020).

[22] R. D. Shannon, Revised effective ionic radii and systematic studies of interatomic distances in halides and chalcogenides, Acta Cryst. **32**, 751 (1976).

[23] ASTM, C1421-10, *Standard Test Methods for Determination of Fracture Toughness of Advanced Ceramics at Ambient Temperature* (ASTM International, West Conshohocken 2010).

[24] T. To, S. S. Sørensen, M. Stepniewska, A. Qiao, L. R. Jensen, M. Bauchy, Y. Yue, and M. M. Smedskjaer, Fracture toughness of a metal-organic framework glass, Nat. Commun. **11**, 2593 (2020).

[25] T. To, F. Célarié, C. Roux-Langlois, A. Bazin, Y. Gueguen, H. Orain, M. le Fur, V. Burgaud, and T. Rouxel, Fracture toughness, fracture energy and slow crack growth of glass as investigated by the single-edge precracked beam (SEPB) and chevron-notched beam (CNB) methods, Acta Mater. **146**, 1 (2018).

[26] J. E. Scrawley, Wide range stress intensity factor expressions for ASTM E 399 standard fracture toughness specimens, Int. J. Fract. **12**, 475 (1976).

[27] A. K. Soper and E. R. Barney, Extracting the pair distribution function from white-beam x-ray total scattering data, J. Appl. Cryst. **44**, 714 (2011).

[28] D. A. Keen, A comparison of various commonly used correlation functions for describing total scattering, J. Appl. Cryst. **34**, 172 (2001).

[29] A. K. Soper, *GudrunN and GudrunX: Programs for Correcting Raw Neutron and X-Ray Total Scattering Data to Differential Cross Section* (Science & Technology Facilities Council, Swindon, 2011).

[30] W. M. Brown, P. Wang, S. J. Plimpton, and A. N. Tharrington, Implementing molecular dynamics on hybrid high performance computers—Short range forces, Comput. Phys. Commun. **182**, 898 (2011).

[31] S. Plimpton, Fast parallel algorithms for short-range molecular dynamics, J. Comput. Phys. **117**, 1 (1995).

[32] S. Sundararaman, L. Huang, S. Ispas, and W. Kob, New interaction potentials for borate glasses with mixed network formers, J. Chem. Phys. **152**, 104501 (2020).

[33] S. Le Roux and P. Jund, Ring statistics analysis of topological networks: New approach and application to amorphous GeS_2 and SiO_2 systems, Comput. Mater. Sci. **49**, 70 (2010).

[34] S. Le Roux and P. Jund, Erratum: Ring statistics analysis of topological networks: New approach and application to amorphous GeS_2 and SiO_2 systems [Comput. Mater. Sci. **49**, 70 (2010)], Comput. Mater. Sci. **50**, 1217 (2011).

[35] S. R. Elliott, The origin of the first sharp diffraction peak in the structure factor of covalent glasses and liquids, J. Phys.: Condens. Matter **4**, 7661 (1992).

[36] Y. Shi, J. Neuefeind, D. Ma, K. Page, L. A. Lamberson, N. J. Smith, A. Tandia, and A. P. Song, Ring size distribution in silicate glasses revealed by neutron scattering first sharp diffraction peak analysis, J. Non-Cryst. Solids **516**, 71 (2019).

[37] C. Crupi, G. Carini, M. González, and G. D'Angelo, Origin of the first sharp diffraction peak in glasses, Phys. Rev. B **92**, 134206 (2015).

[38] C. J. Benmore, R. T. Hart, Q. Mei, D. L. Price, J. Yarger, C. A. Tulk, and D. D. Klug, Intermediate range chemical ordering in amorphous and liquid water, Si, and Ge, Phys. Rev. B **72**, 132201 (2005).

[39] C. Prescher, V. B. Prakapenka, J. Stefanski, S. Jahn, L. B. Skinner, and Y. Wang, Beyond sixfold coordinated Si in SiO_2 glass at ultrahigh pressures, Proc. Natl. Acad. Sci. USA **114**, 10041 (2017).

[40] C. J. Benmore, E. Soignard, S. A. Amin, M. Guthrie, S. D. Shastri, P. L. Lee, and J. L. Yarger, Structural and topological changes in silica glass at pressure, Phys. Rev. B **81**, 054105 (2010).

[41] Q. Zhou, Y. Shi, B. Deng, J. Neuefeind, and M. Bauchy, Experimental method to quantify the ring size distribution in silicate glasses and simulation validation thereof, Sci. Adv. **7**, eabh1761 (2021).

[42] V. F. Sears, Neutron scattering lengths and cross sections, Neutron News **3**, 26 (1992).

[43] S. Sundararaman, L. Huang, S. Ispas, and W. Kob, New interaction potentials for alkali and alkaline-earth aluminosilicate glasses, J. Chem. Phys. **150**, 154505 (2019).

[44] H. Liu, B. Deng, S. Sundararaman, Y. Shi, and L. Huang, Understanding the response of aluminosilicate and aluminoborate glasses to sharp contact loading using molecular dynamics simulation, J. Appl. Phys. **128**, 035106 (2020).

[45] R. Christensen, S. S. Sørensen, H. Liu, K. Li, M. Bauchy, and M. M. Smedskjaer, Interatomic potential parameterization using particle swarm optimization: case study of glassy silica, J. Chem. Phys. **154**, 134505 (2021).

[46] H. Hashimoto, Y. Onodera, S. Tahara, S. Kohara, K. Yazawa, H. Segawa, M. Murakami, and K. Ohara, Structure of alumina glass, Sci. Rep. **12**, 516 (2022).

[47] Y. Yang, H. Tokunaga, M. Ono, K. Hayashi, and J. C. Mauro, Thermal expansion of silicate glass-forming systems at high

temperatures from topological pruning of ring structures, J. Am. Ceram. Soc. **103**, 4256 (2020).

[48] Y. Shih, S. Sundararaman, and L. Huang, Structural origin of the anomalous density maximum in silica and alkali silicate glasses, J. Am. Ceram. Soc. **103**, 3942 (2020).

[49] J. Yang, Y. Kim, and I. Sohn, Gaining insights on high-temperature thermal conductivity and structure of oxide melts through experimental and molecular dynamics simulation study, J. Mater. Res. Technol. **10**, 268 (2021).

[50] X. Ren, T. Du, H. Peng, L. R. Jensen, C. A. N. Biscio, L. Fajstrup, M. Bauchy, and M. M. Smedskjaer, Irradiation-induced toughening of calcium aluminoborosilicate glasses, Mater. Today Commun. **31**, 103649 (2022).

[51] R. E. Youngman and J. W. Zwanziger, Multiple boron sites in borate glass detected with dynamic angle spinning nuclear magnetic resonance, J. Non-Cryst. Solids **168**, 293 (1994).

[52] J. Krogh-Moe, The structure of vitreous and liquid boron oxide, J. Non-Cryst. Solids **1**, 269 (1969).

[53] C. F. Windisch and W. M. Risen, Vibrational spectra of oxygen- and boron-isotopically substituted B_2O_3 glasses, J. Non-Cryst. Solids **48**, 307 (1982).

[54] J. Goubeau and H. Keller, RAMAN-Spektren und Struktur von Boroxol-Verbindungen, Z. Anorg. Allg. Chem. **272**, 303 (1953).

[55] K. Januchta, M. Stepniewska, L. R. Jensen, Y. Zhang, M. A. J. Somers, M. Bauchy, Y. Yue, and M. M. Smedskjaer, Breaking the limit of micro-ductility in oxide glasses, Adv. Sci. **6**, 1901281 (2019).

[56] G. Ferlat, T. Charpentier, A. P. Seitsonen, A. Takada, M. Lazzeri, L. Cormier, G. Calas, and F. Mauri, Boroxol Rings in Liquid and Vitreous B_2O_3 from First Principles, Phys. Rev. Lett. **101**, 065504 (2008).

[57] J. K. Maranas, Y. Chen, D. K. Stillinger, and F. H. Stillinger, Polarization interactions and boroxol ring formation in boron oxide: A molecular dynamics study, J. Chem. Phys. **115**, 6578 (2001).

[58] Q. Mei, C. J. Benmore, S. Sen, R. Sharma, and J. L. Yarger, Intermediate range order in vitreous silica from a partial structure factor analysis, Phys. Rev. B **78**, 144204 (2008).

[59] H. Singh, Q. Shu, G. King, Z. Liang, Z. Wang, W. Cao, M. Huttula, and T. Fabritius, Structure and viscosity of CaO–Al_2O_3–B_2O_3–BaO slags with varying mass ratio of BaO to CaO, J. Am. Ceram. Soc. **104**, 4505 (2021).

[60] T. Du, S. S. Sørensen, T. To, and M. M. Smedskjaer, Oxide glasses under pressure: Recent insights from experiments and simulations, J. Appl. Phys. **131**, 170901 (2022).

[61] J. Wu, J. Deubener, J. F. Stebbins, L. Grygarova, H. Behrens, L. Wondraczek, and Y. Yue, Structural response of a highly viscous aluminoborosilicate melt to isotropic and anisotropic compressions, J. Chem. Phys. **131**, 104504 (2009).

[62] M. N. Svenson, M. Guerette, L. Huang, N. Lönnroth, J. C. Mauro, S. J. Rzoska, M. Bockowski, and M. M. Smedskjaer, Universal behavior of changes in elastic moduli of hot compressed oxide glasses, Chem. Phys. Lett. **651**, 88 (2016).

[63] A. Makishima and J. D. Mackenzie, Direct calculation of Young's modulus of glass, J. Non-Cryst. Solids **12**, 35 (1973).

[64] K. Yang, B. Yang, X. Xu, C. Hoover, M. M. Smedskjaer, and M. Bauchy, Prediction of the Young's modulus of silicate glasses by topological constraint theory, J. Non-Cryst. Solids **514**, 15 (2019).

[65] J. Wu, T. M. Gross, L. Huang, S. P. Jaccani, R. E. Youngman, S. J. Rzoska, M. Bockowski, S. Bista, J. F. Stebbins, and M. M. Smedskjaer, Composition and pressure effects on the structure, elastic properties and hardness of aluminoborosilicate glass, J. Non-Cryst. Solids **530**, 119797 (2020).

[66] A. Makishma and J. D. Mackenzie, Calculation of bulk modulus, shear modulus and Poisson's ratio of glass, J. Non-Cryst. Solids **17**, 147 (1975).

[67] T. Rouxel, Fracture surface energy and toughness of inorganic glasses, Scr. Mater. **137**, 109 (2017).

[68] Y. Yue, L. Wondraczek, H. Behrens, and J. Deubener, Glass transition in an isostatically compressed calcium metaphosphate glass, J. Chem. Phys. **126**, 144902 (2007).

[69] L. Wondraczek, H. Behrens, Y. Yue, J. Deubener, and G. W. Scherer, Relaxation and glass transition in an isostatically compressed diopside glass, J. Am. Ceram. Soc. **90**, 1556 (2007).